$Li_2S-P_2S_5$. The compositional dependence of the NMR and X-ray data consistently indicates the existence of four pseudobinary crystalline compounds with the stoichiometries $LiPS_3$, $Li_4P_2S_6$, Li_3PS_4, and Li_7PS_6, whose structural environments have been characterized by anisotropic solid-state NMR chemical shielding parameters. With the exception of Li_3PS_4, the structural arrangements existing in these crystalline compounds have no counterpart in the analogous oxide system $Li_2O-P_2O_5$.

The results of the present study emphasize the significance of non-oxide chalcogenide glasses from the viewpoint of structural chemistry. Contrary to oxide glasses, which can be viewed as random arrangements of local environments already known in crystalline compounds, chalcogenide glasses show local environments unique to the glassy state that appear unstable in the crystalline form. Overall, the glassy state tends to favor connectivities more analogous to those present in oxidic glasses; i.e., corner-sharing is favored over edge-sharing and dimeric

thiopyrophosphate groups are favored over the hexathiohypodiphosphate units. Current NMR investigations focus on the question of how this distribution of structural units can be influenced by coformers such as Al_2S_3, B_2S_3, and SiS_2. This question is relevant with respect to the role these coformers play in determining the stability of the solid electrolyte against the lithium anode materials in battery cells.[69,70]

(69) Kennedy, J. H.; Zhang, Z. *Solid State Ionics* **1988** *28–30*, 726.
(70) Kennedy, J. H.; Zhang, Z. *J. Electrochem. Soc.* **1989**, *136*, 2441.

Electron Microscopy Study of Delamination in Dispersions of the Perovskite-Related Layered Phases $K[Ca_2Na_{n-3}Nb_nO_{3n+1}]$: Evidence for Single-Layer Formation

M. M. J. Treacy,* S. B. Rice, A. J. Jacobson,* and J. T. Lewandowski

Exxon Research and Engineering Company, Annandale, New Jersey 08801

Received November 27, 1989

Intercalation of basic surfactant molecules into the layered perovskites $H[Ca_2Na_{n-3}Nb_nO_{3n+1}]$, $n = 3$–5, can be used to cause spontaneous exfoliation of the structure into thin sheets that form stable dispersions in a polar solvent. The extent of exfoliation has been determined by examining Rutherford scattered intensities into a high-angle annular dark-field detector in a scanning transmission electron microscope. It is shown that for $n \leq 5$, the layered perovskites can be exfoliated to form single layers. Exfoliation is easiest for the $n = 3$ and 4 materials.

Introduction

A series of compounds, $A[Ca_2Na_{n-3}Nb_nO_{3n+1}]$ (A = K, Rb, Cs), $n = 3$–7,[1-4] has recently been shown to have perovskite-related layered structures, as illustrated schematically in Figure 1 for the potassium compound with $n = 3$. The detailed structure has been determined for one of the end members, $Cs[Ca_2Na_{n-3}Nb_nO_{3n+1}]$, $n = 3$.[2] The structure comprises perovskite-like layers of NbO_6 octahedra that are terminated along one of the perovskite cubic directions. The layers are n octahedra thick and contain $n - 1$ cations that are all calcium atoms when $n = 3$ or disordered sodium and calcium atoms when $n > 3$. Other related compounds, $KLnNb_2O_7$ (Ln = La, Nd),[4,5] $A_2Ln_2Ti_3O_{10}$ (A = Na, K, Rb and Ln = La, Nd, Sm, Gd, Dy),[6,7] and $ABiNb_2O_7$ and $APb_2Nb_3O_{10}$ (A = Rb, Cs)[8] have recently been described. An unusual feature of all of these

phases is that they readily ion exchange the interlayer cations. Exchange has been observed in molten salts[1] and by treatment in aqueous acid at ambient to slightly elevated temperatures.[1,3-9] In the latter case, the compounds formed, for example, the $H[Ca_2Na_{n-3}Nb_nO_{3n+1}]$ series, are solid acids and can react further with organic bases to form intercalation compounds with large interlayer expansions.[10] Insertion of long-chain organic amines between the perovskite layers produces a large volume expansion, and individual crystallites begin to exfoliate to form sheets that are very thin in the direction perpendicular to the layers. A scanning electron micrograph (Figure 2) of a crystal of $H[Ca_2Nb_3O_{10}]$ that has been intercalated with octadecylamine shows the beginning stages of layer separation. The limiting case of this process is the complete breakdown of the crystal into single layers. The phenomenon is known to occur in several systems, particularly in the smectite clay minerals, which are well known to spontaneously exfoliate in water.[11] Other systems with comparable layer charges behave similarly, e.g., Na_xMS_2,[12-14] $FeOCl$,[15] and

(1) Dion, M.; Ganne, M.; Tournoux, M. *Mater. Res. Bull.* **1981**, *16*, 1429–1435.
(2) Dion, M.; Ganne, M.; Tournoux, M. *Rev. Chim. Mineral.* **1984**, *21*, 92–103.
(3) Jacobson, A. J.; Johnson, J. W.; Lewandowski, J. T. *Inorg. Chem.* **1985**, 3727–3729.
(4) Dion, M.; Ganne, M.; Tournoux, M. *Rev. Chim. Mineral.* **1986**, *23*, 61–69.
(5) Gopalakrishnan, J.; Bhat, V.; Raveau, B. *Mater. Res. Bull.* **1987**, *22*, 413–417.
(6) Gondrand, M.; Joubert, J.-C. *Rev. Chim. Mineral.* **1987**, *24*, 33–41.
(7) Gopalakrishnan, J.; Bhat, V. *Inorg. Chem.* **1987**, *26*, 4299–4301.
(8) Subramanian, M. A.; Gopalakrishnan, J.; Sleight, A. W. *Mater. Res. Bull.* **1988**, *23*, 837–842.

(9) Jacobson, A. J.; Lewandowski, J. T.; Johnson, J. W. *J. Less Common Met.* **1986**, *116*, 137–146.
(10) Jacobson, A. J.; Johnson, J. W.; Lewandowski, J. T. *Mater. Res. Bull.* **1987**, *22*, 45–51.
(11) Grim. R. E. *Clay Mineralogy*, 2nd ed.; McGraw-Hill: New York, 1968.
(12) Lerf, A.; Schollhorn, R. *Inorg. Chem.* **1977**, *16*, 2950–2956.
(13) Murphy, D. W.; Hull, Jr., G. W. *J. Chem. Phys.* **1975**, *62*, 973–978.

280 *Chem. Mater., Vol. 2, No. 3, 1990*

Treacy et al.

Table I. Intercalation Compounds of H[Ca$_2$Na$_{n-3}$Hb$_n$O$_{3n+1}$] with M360 and M600 Amines

n	G^a	G/H	temp, °C	time, h	x	c, nm	Δc, nm
3	M360	5.0	90	87	0.58	6.330	4.89
3	M600	2.9	60	111	0.53	4.010	2.57
					0.51	3.365^b	1.93
4	M360	5.0	60	89	0.40	4.429	2.59
5	M360	5.6	60	111	0.33	4.620	2.40

^{a}G is the intercalating amine and H and n refer to the host perovskite lattice H[Ca$_2$Na$_{n-3}$Nb$_n$O$_{3n+1}$]. ^{b} corresponds to the n = 3, M600 sample heated at 100 °C.

○ Oxygen

● Niobium

◕ Calcium

▨ Potassium
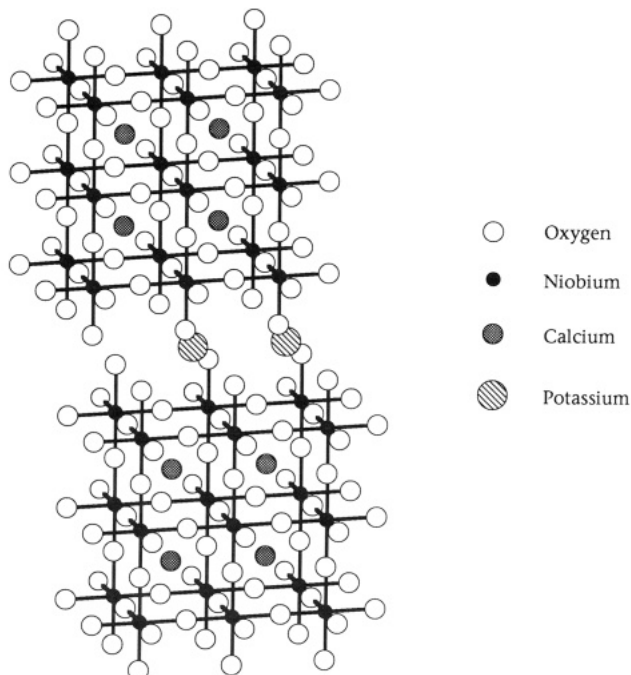
Figure 1. Schematic representation of two layers of the structure of K[Ca$_2$Na$_{n-3}$Nb$_n$O$_{3n+1}$], n = 3.

M$_x$MPS$_3$.[16] Recently, the synthesis of single MoS$_2$ layers by reaction of the lithium intercalation compound with water has been described.[17,18] The final layer charge is uncertain in this system since some layer hydrolysis is reported to occur. Exfoliation of layered compounds with higher layer charges is more difficult but has been achieved by preintercalation of a molecule which weakens the interlayer bonding. Short-chain primary amines (C$_3$–C$_4$) have been used successfully to promote exfoliation of vermiculite,[19] Zr(HPO$_4$)$_2$·2H$_2$O,[20] and HTiNbO$_5$.[21] In the case of H[Ca$_2$Nb$_3$O$_{10}$], the layer charge is very high (0.147 nm^2/e), and further modification of the layer surfaces is necessary to induce similar exfoliation. The modification is achieved by interlayer protonation of the amine head group of a surfactant molecule, which contains a hydrophilic polyether tail. When intercalated, the surfactant enhances the interaction of solvent molecules with the interlayer space and facilitates exfoliation. A similar strategy for the exfoliation of Zr(RPO$_3$)$_2$ layers using polyether R groups has been reported.[22]

Proof that exfoliation occurs at the single sheet level is difficult to obtain. Because of their high aspect ratio, sheets will lie on transmission electron microscope (TEM) grids almost exclusively in plan view, with sheet normals toward the beam direction, and edgewise views being very rare. Intensities from conventional bright-field and dark-field images are difficult to interpret quantitatively in terms of thickness, due to the complex interplay of phase and amplitude contrasts that form the image. Occasional folded sheets will provide glimpses of layer thickness but not in any sufficiently quantitative way. Many TEM studies of clay particles have demonstrated the presence of thin sheets of the order of 1–2 layers thick using low-angle shadowing methods to measure sheet thicknesses.[23,24] However, the resolution of this method is limited by delineation of the crystal and shadow edges and by the assumption that the individual particles lie flat on the substrate.

In this paper the synthesis of exfoliated layered perovskites is described, together with a new imaging technique for characterizing the extent of the exfoliation. The technique measures the distribution of Rutherford scattered intensities into a high-angle annular detector in a scanning transmission electron microscope (STEM). Oxide layer thickness is deduced directly from the intensity of scattering, as the signal is proportional to specimen mass thickness. The technique is insensitive to sheet buckling, it measures thickness at all points across a sheet rather than only at the edge, and it obtains thickness distributions directly from the intensity histogram of a single image.

Experimental Section

Preparation of the Oxide Dispersions. The layered perovskites, K[Ca$_2$Na$_{n-3}$Nb$_n$O$_{3n+1}$], n = 3–5, were prepared and converted to the proton-exchanged forms as described previously.[3,9] The proton-exchanged forms were then intercalated with monoamine surfactant molecules. Two specific types were used, both of which were obtained from Texaco and are designated "Jeffamine" M360 and M600. The surfactants have average compositions represented by n-C$_4$H$_9$(OCH$_2$CH$_2$)$_4$(OCH$_2$CH-(CH$_3$))$_2$NH$_2$ and by CH$_3$OC$_2$H$_4$(CH$_3$CH(CH$_3$)O)$_8$CH$_2$CH(CH$_3$)N-H$_2$ for the M360 and M600 materials, respectively. Both materials have a monoamine head group that can be protonated by the interlayer cations and a hydrophilic tail that enhances the affinity of the interlayer space for polar molecules.

The intercalation reactions were carried out by heating an aqueous solution of the M360 or M600 surfactant with the solid layered compound. The reaction conditions are sumarized in Table I. An excess of the surfactant over that required for complete neutralization of the interlayer protons was used (G/H in Table I). After the reaction, the solid products were recovered by filtration, washed well with excess water, and dried under vacuum at room temperature. Intercalation was confirmed by powder X-ray diffraction measurements on the dried powder samples using a Siemens D500 diffractometer and Cu Kα radiation. X-ray measurements were also made on oriented films that

(14) Nazar, L. F.; Jacobson, A. J. *J. Chem. Soc., Chem. Commun.* **1986**, 570–571.

(15) Weiss, A.; Sick, E. *Z. Naturforsch.* **1978**, *33b*, 1087–1090.

(16) Clement, R.; Garnier, O.; Jegoudez, J. *Inorg. Chem.* **1986**, *25*, 1404–1409.

(17) Divaigalpitiya, W. M. R.; Frindt, R. F.; Morrison, S. R. *Science* **1989**, *246*, 369–371.

(18) Joensen, P.; Frindt, R. F.; Morrison, S. R. *Mater. Res. Bull.* **1986**, *21*, 457–461.

(19) Ballard, D. G. H.; Rideal, G. R. *J. Mater. Sci.* **1983**, *18*, 545–561.
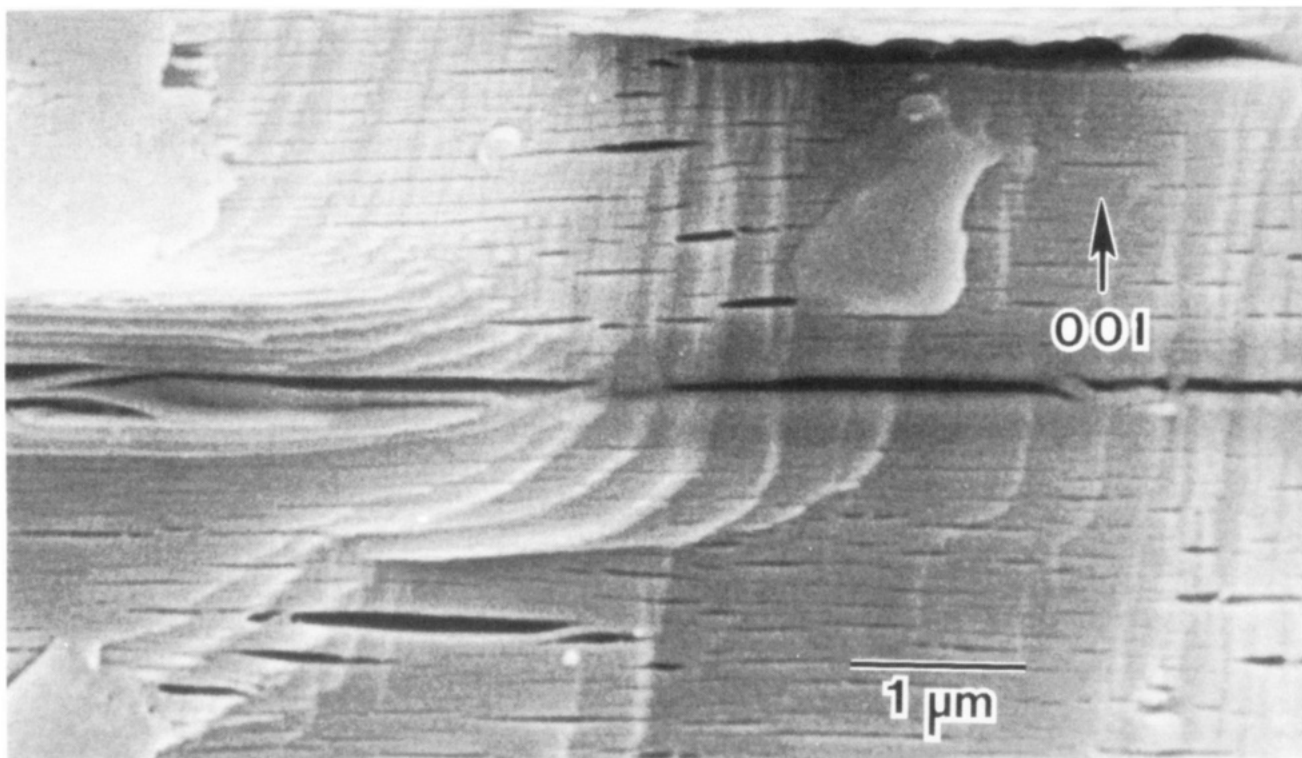
(20) Alberti, G.; Casciola, M.; Costantino, U. *J. Colloid Interfacial Sci.* **1985**, *107*, 256–263.

(21) Rebbah, H.; Borel, M. M.; Raveau, B. *Mater. Res. Bull.* **1980**, *15*, 317–321.

(22) Ortiz-Avila, C. Y.; Clearfield, A. *Inorg. Chem.* **1985**, *24*, 1733–1778.

(23) Nadeau, P. H.; Tait, J. M.; McHardy, W. J.; Wilson, M. J. *Clay Minerals* **1984**, *19*, 67–76.
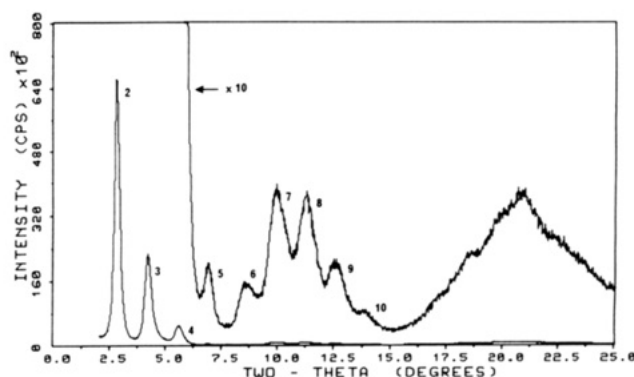
(24) Weir, A. H.; Nixon, H. L.; Woods, R. D. *Clays Clay Minerals* **1962**, *9*, 419–423.

Figure 2. Scanning electron micrograph of a crysal of $H[Ca_2Nb_3O_{10}]$ that had been intercalated with octadecylamine showing the beginning stages of layer separation or exfoliation.

were prepared by dropping a dispersion of the sample onto a glass slide and allowing it to dry. The X-ray data from the powder samples indicate the formation of single phases, though in a few reactions small amounts of a phase with a *c* axis length of 1.5 nm was observed. It is likely that this corresponds to the phase $NH_4Ca_2Nb_3O_{10}$ possibly formed through some thermal decomposition of the surfactant. The X-ray data of the intercalation compounds, in general, show $00l$ and $hk0$ lines but no mixed (hkl) reflections. The $hk0$ lines indicate that all of the intercalation compounds remain tetragonal with $a = 0.3865$ (5) nm. Intercalation results in a substantial increase in the measured *c* axis spacings above the values for the starting materials (Table I). The compounds with the M360 amine give comparable lattice expansions, which are smaller than the increase observed for the compound formed by reaction of the $n = 3$ oxide with the larger M600 amine. The precise values of the interlayer separations are sensitive to the drying conditions used in the preparation as indicated by the ~ 0.65-nm reduction in *c* axis spacing observed for the $n = 3$, M360 phase after heating at 100 °C. Similar large changes in the interlayer separation have been observed previously for the *n*-alkylammonium intercalation compounds[10] and are associated with conformational changes in the organic molecule chain. The X-ray data from an oriented film of the $n = 3$, M600 phase are shown in Figure 3. The $00l$ lines out to $l = 10$ are clearly identified, although the line positions deviate in a systematic way from the values calculated from the average interlayer separation. The deviations are characteristic of disorder due to random stacking of two different interlayer spacings, usually referred to in clay chemistry as interstratification,[25] and may indicate variations in surfactant content between different interlayers within one crystallite.

The compositions of the intercalation compound, expressed as $H[Ca_2Na_{n-3}Nb_nO_{3n+1}] \cdot x$M360 or xM600 (Table I), were determined by thermogravimetric (TGA) oxidation in air to 1000 °C using a Du Pont 1090 thermal analyzer. The preparation procedure described above results in the formation of phases with negligible water content, and the major weight loss in the TGA scans (centered at 300 °C) corresponds to the oxidation of the organic intercalant. The measured compositions (x) decrease with

(25) Reynolds, R. C. *Interstratified Clay Minerals*; Brindley, G. W., Brown, G., Eds.; Mineralogical Society: London, 1980; pp 249–303.

Figure 3. X-ray diffraction pattern of an oriented film of $H[Ca_2Nb_3O_{10}] \cdot$M600. The intensity scale has been expanded by a factor of 10 in the right-hand part of the figure; the integers refer to the $00l$ index.

increasing *n*. Exfoliation of the intercalation compounds was achieved by suspending the solids (50–100 mg) in water (30 mL) for the M360 phases or in acetone for the M600 compound, which does not disperse in water. The suspensions were then placed in an ultrasonic cleaning bath for 5–15 min to induce the maximum extent of exfoliation. The dispersions were further diluted to 100 mL and allowed to settle for several hours. The larger particles sedimented, but a substantial amount of the solids remained dispersed. The decanted dispersions were stable for several days and were used to prepare the samples for electron microscopy. It was observed that the $n = 4$ and $n = 5$ compounds dispersed less readily than the $n = 3$ material, which may be related to their slightly lower surfactant contents.

Electron Microscopy

High-Angle Annular Detector Imaging in the STEM. The conventional bright-field transmission electron microscope (TEM) forms a fixed-beam image where image intensity results from a complicated interplay of amplitude and phase contrasts. On the other hand, the scanning transmission electron microscope (STEM) forms images by rastering a finely focused probe across the

282 *Chem. Mater., Vol. 2, No. 3, 1990*

Treacy et al.

specimen. Since the specimen is now being analyzed on a point-by-point basis, there is greater opportunity for selecting a specific scattering mechanism with which to form an image. The high-angle annular detector (HAAD) signal in the STEM is dominated by electrons that have been elastically scattered from the atomic nuclei of the specimen.[26-29] For 100-kV electrons, this corresponds to scattering angles beyond about 0.1 rad. Electron diffraction from thin crystals is weak at these angles, since atomic thermal vibration amplitudes are comparable to the spacings of those planes spaced closely enough to diffract kinematically into the annular detector. Dynamical diffraction effects are negligible when the crystals are thin, so multiple diffraction and electron channeling effects (for probes comparable to, or larger than the unit cell dimensions) can be ignored.

Under these conditions, the HAAD signal at a point in the specimen is proportional to

$$I_{HAAD} = (\pi\delta^2 t I_0/4)\sum_i \sigma_i/\Omega_i \qquad (1)$$

where δ is the diameter of the electron probe, t the crystal thickness, Ω_i the average specimen volume per atom of type i, and I_0 the incident current in electrons per unit area. The scattering cross section σ_i, for scattering into the annular detector, comprises both elastic and inelastic components. At large angles, the ratio of elastic to inelastic scattering is approximately proportional to the atomic number,[30] Z, and the contribution due to inelastic scattering is usually ignored.

There are many theoretical models for elastic scattering of electrons discussed in the literature[31,32] but very few quantitative studies for scattering into annular detectors. Pennycook et al.[33] found that the empirical model by Fleischmann[34] gave the best overall fit to their HAAD data for scattering from As, Sb, and Bi dopants in thin Si specimens. Although the model overestimates absolute scattered intensities by 10-20% for these elements, the behavior of the scattering with respect to the annular detector inner collection angle closely paralleled their data.

The Fleischmann formula was based on an empirical fit to calculations by Molière,[35] who showed that the Born approximation seriously underestimates the effects of screening in high-Z atoms at large scattering angles. For scattering into an annular detector with inner and outer collection angles of θ_1 and θ_2, respectively, the Fleischmann cross section is[33]

$$\sigma_i = \left(\frac{m}{m_0}\right)^2 \frac{Z^2\lambda^4}{2\pi^2 a_0^2}\left[\frac{\theta_2-\theta_1}{\theta_1\theta_2\theta_\alpha} + \frac{1}{\theta_\alpha^2}\ln\left(\frac{\theta_1}{\theta_2}\frac{\theta_2+\theta_\alpha}{\theta_1+\theta_\alpha}\right)\right] \qquad (2)$$

where a_0 is the Bohr radius and θ_α is a term that models the screening of the nuclear charge by orbital electrons. θ_α is given by

$$\theta_\alpha = \frac{1.13Z^{1/3}}{137\beta}\left[1.13 + 3.76\left(\frac{Z}{137\beta}\right)^2\right]^{1/2}\exp(1/2) \qquad (3)$$

Here, $\beta = v/c$, the ratio of the velocity of the incoming electron to the velocity of light, and Z is the atomic number. m_0 is the rest mass of the electron, which has effective mass m at velocity v, and λ is the effective wavelength of the incoming electron.

The Z dependence of the elastic scattering increases as the inner collection angle θ_1 increases (assuming $\theta_1 < \theta_2 < \pi$), tending asymptotically to the full Z^2 of the classical Rutherford formula as $\theta_1 \rightarrow \pi$. This strong Z dependence has made HAAD imaging an attractive method for analyzing inhomogeneous distributions of high-Z materials in low-Z matrices. Frequently referred to as Z contrast, HAAD imaging has been used for studying single-atom diffusion on thin supports,[36] for detecting and measuring subnanometer Pt catalyst particles on alumina and zeolite supports,[26,37] for mapping trace concentrations of high Z impurities,[33,38] and most recently for directly imaging the variation of average atomic number within crystal unit cells, such as YBa$_2$Cu$_3$O$_{7-\delta}$[39] and Si/Ge$_x$Si$_{1-x}$ superlattices.[40]

In the results presented here, we take advantage of two important features of the HAAD signal. The first is the sensitivity of the HAAD signal to atomic number, which is important for the initial detection of the sheets against the carbon support film background. The second is the linearity of the scattered intensity with respect to specimen mass thickness (see eq 1). This latter property enables relative sheet thicknesses to be estimated.

Specimen Preparation and Experimental Electron Microscopy. Samples for electron microscopy were prepared by dipping copper grids, coated with stress-free continuous carbon, into the sedimented dispersions and allowing them to dry in air.[41] The concentrations of the dispersions were adjusted by progressive dilution in order to limit the number of overlapping particles on the grids. The electron microscopy was carried out using a Vacuum Generators HB501A STEM fitted with a high-angle annular detector (inner collection semiangle of about 0.1 rad, outer semiangle of about 0.3 rad, giving a nominal $\sim Z^{1.85}$ signal dependence). The image data were recorded digitally in 512 × 512 × 8 bit deep pixel arrays and analyzed by using a Tracor Northern 5700 image-processing system. Before examination, the samples were heated under vacuum (10^{-8} bar) at 500 °C in a sample treatment antechamber and then inserted into the microscope. This baking procedure was necessary to stabilize the samples against contamination under the electron beam. Evidence presented in the results section indicates that, on heating, surfactant associated with the oxide layers is broken down to form a stable carbonaceous layer over the sample.

Several samples with different values of n were examined separately. However, the most detailed comparison was made between samples exfoliated by using M360 in water, with $n = 3$ and 4. Samples were separately loaded

(26) Treacy, M. M. J.; Howie, A.; Wilson, C. J. *Philos. Mag.* 1978, *A38*, 569–585.

(27) Treacy, M. M. J. Howie, A.; Pennycook, S. J. In Mulvey, T., Ed.; Inst. Phys. Conf. Ser., London, 1980; Vol. 52, p 251.

(28) Humphreys, C. J.; Sandström, R.; Spencer, J. P. In *Scanning Electron Microsc/1973*; part II, IIT Research Institute, Chicago, 1973; pp 233–241.

(29) Crewe, A. V.; Langmore, J. P.; Isaacson, M. S. In *Physical Aspects of Electron Microscopy and Microbeam Analysis*; Siegel, B. M., Beaman, D. R., Eds.; Wiley: New York, 1975; pp 47–62.

(30) Landau, L. D.; Lifshitz, E. M. *Quantum Mechanics (Non-relativistic Theory)*; Pergamon Press: New York, 1977; pp 627.

(31) Motz, J. W.; Olsen, H.; Koch, H. W. *Rev. Mod. Phys.* 1964, *36*, 881–928.

(32) Scott, W. T. *Rev. Mod. Phys.* 1963, *35*, 231–313.

(33) Pennycook, S. J.; Berger, S. D.; Culbertson, R. J. *J. Microsc.* 1986, *144*, 229–249.

(34) Fleischmann, H. *Z. Naturforsch.* 1960, *15a*, 1090–1096.

(35) Molière, G. *Z. Naturforsch.* 1947, *2a*, 133.

(36) Isaacson, M. S; Ohtsuki, M.; Utlaut, M. In *Introduction to Analytical Electron Microscopy*; Hren, J. J., Goldstein, J. I., Joy, D. C., Eds.; Plenum Press: New York, 1979; pp 343–368.

(37) Treacy, M. M. J.; Rice, S. B. *J. Microsc.* 1989, *156*, 211–234.

(38) Treacy, M. M. J.; Gibson, J. M.; Short, K. T.; Rice, S. B. *Ultramicroscopy* 1988, *26*, 133–142.

(39) Pennycook, S. J.; Boatner, L. A. *Nature* 1988, *336*, 565–567.

(40) Pennycook, S. J.; Jesson, D. E.; Chisholm, M. F. *Microscopy of Semiconducting Materials, 1989*; Inst. Phys. Conf. Ser.; Bristol, 1989; Vol. 100, pp 51–58.

(41) Rice, S. B.; Treacy, M. M. J. In *Specimen Preparation Techniques for TEM of Materials*; Bravman, J., McDonald, M., Anderson, R., Eds.; Materials Research Society Symposium Proceedings Pittsburgh, 1988; No. 115, pp 15–28.
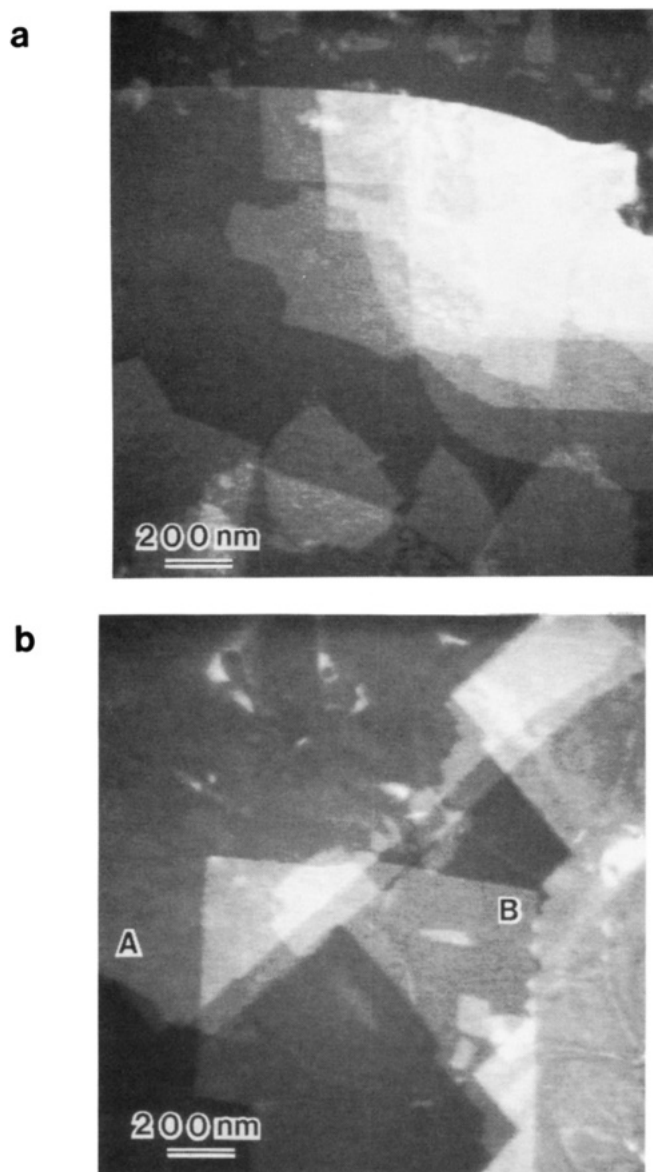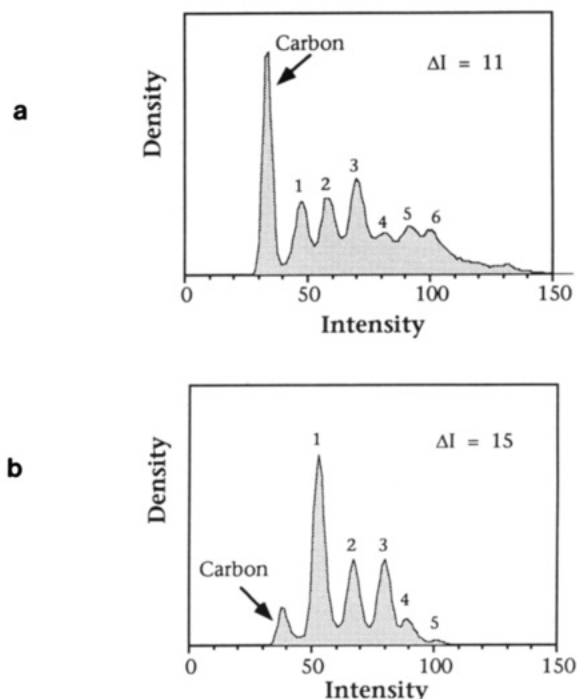
Figure 4. STEM HAAD images of exfoliated sheets of K-[$Ca_2Na_{n-3}Nb_nO_{3n+1}$], lying on amorphous carbon, seen in plan view. The image intensity is a map primarily of the specimen mass-thickness (see eq 1 in text): (a) $n = 3$; (b) $n = 4$.

Figure 5. Intensity histograms of HAAD images of exfoliated sheets of K[$Ca_2Na_{n-3}Nb_nO_{3n+1}$], supported on amorphous carbon. The number above each peak corresponds to the number of overlapping layers contributing to the intensity. Note the quantized steps in intensity, ΔI: (a) $n = 3$, with steps of ≈ 11 intensity units; (b) $n = 4$, with steps of ≈ 15 intensity units.

onto two half-grids and mounted side-by-side in the same sample holder. To distinguish specimens, one half-grid was cut parallel to the grid bars, the other across a diagonal. This configuration enabled a direct comparison to be made under identical instrumental settings. Intensities from the carbon support film were collected for each analyzed area, as well as the hole count, which provides a measure of the shot noise in the detector system. Detector linearity was verified by comparing the form of the intensity histograms at different amplifier and incident beam current settings.

Microscopy Results. STEM specimens frequently had two types of oxide particle, particularly for the $n > 4$ specimens. Large areas of the grid were covered with extremely thin plates oriented almost exclusively in plan view. However, occasional large three-dimensional crystallites were observed. These were too thick for HAAD analysis and were presumed to be large unexfoliated crystallites. It is estimated that at least 95% of the $n = 3$ and 70% of the $n = 4$ perovskite-like materials were present on the microscope grid as exfoliated sheets.

Figure 4 shows dark-field micrographs of these specimens showing the thin layers and varieties of overlapping platelets. Histograms of intensity (Figure 5) provide a test of whether or not the chemical exfoliation procedure splits the materials into discrete layers of integral numbers of layer thicknesses. The histograms have been corrected for the hole count, which was about 20% of the carbon intensity. The peak separations appear to be constant for both materials. For the $n = 3$ material, the sheet intensities increment by approximately ~ 11 intensity units, relative to 32 intensity units for the nominally 20-nm-thick amorphous carbon support film (a ratio of about 34%). For the $n = 4$ material the intensity increments by ~ 15 intensity units, relative to 39 units for the support foil (a ratio of about 38%).

Frequently, sheets in these specimens have regions (usually at the sheet corners or sides) where extra layers were coherently attached in a stepped configuration. Figure 4a shows such a region on the $n = 3$ specimen. Such images suggest that the intercalation of surfactant molecules between the layers is not uniform and that some layers are finally separated by ripping, with the unintercalated areas being left attached.

The quantized intensity increments between oxide peaks make a persuasive qualitative argument that we are looking at single-sheet increments in layer thickness, with the lowest intensity sheets corresponding to single layers. This interpretation has been confirmed by rare side views of folded sheets in the STEM bright-field image (which can be viewed simultaneously with the HAAD image). However, side views are too infrequent to be used routinely to measure thickness distributions. To unambiguously determine sheet thickness from the intensity data, it is necessary to establish the intensity expected from one oxide sheet relative to the nominally 20-nm-thick carbon support foil. Figure 6 shows the results of applying the Fleishmann formula (eqs 2 and 3) to scattering from single sheets of H[$Ca_2Na_{n-3}Nb_nO_{3n+1}$] for $n = 3–5$. The results are plotted as a ratio of scattered intensity from a single
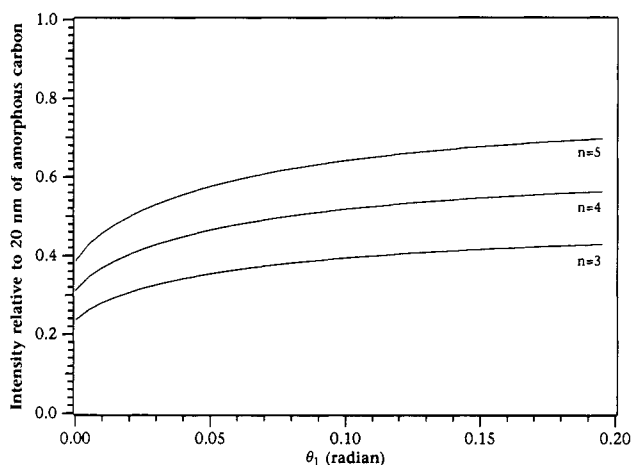
Figure 6. Calculated intensity of single sheets of K-$[Ca_2Na_{n-3}Nb_nO_{3n+1}]$ relative to 20 nm of amorphous carbon, for $n = 3-5$, using the Fleischmann elastic scattering cross section of eq 2.

Table II. Experimental and Calculated Data Used as Input to Eqs 5 and 6

|		$n = 3$	$n = 4$
exptl	$I_{HAAD}(1)/I_{HAAD}(0)$	0.34	0.38
calcn	I_{oxide}/I_{carbon}	0.42	0.54

sheet relative to a 20-nm-thick amorphous carbon support film, as a function of the annular detector inner collection angle θ_1, and with θ_2 fixed at 0.3 radian.

Figure 6 indicates that the $n = 3$ and 4 materials should scatter respectively 40% and 52% as strongly as 20 nm of carbon. Thus the experimental intensity increments are systematically lower than the calculations predict for single sheets by as much as 25%. Furthermore, experimentally, the $n = 4$ material scatters only 15% more strongly than the $n = 3$ material. Calculation predicts that $n = 4$ should scatter $\sim 30\%$ more strongly than $n = 3$. The results of data and calculation are summarized in Table II. Figure 6 shows that the ratio of scattering strengths between layers does not depend sensitively on the precise value of θ_1.

The discrepancies between experiment and calculation most probably arise from the presence of an extra carbonaceous deposit, resulting from the decomposition of surfactant molecules when the specimen is baked. It is unlikely that fluctuations in carbon support foil thickness alone can account for the discrepancy. The error in the absolute thickness of the carbon foils was measured conservatively to be 20 nm ± 10%, as deduced from plasmon energy loss measurements on representative carbon foils. Furthermore, variability in thickness between carbon foils prepared in the same batch is probably much less than 10%.

Close inspection of intensity histograms reveals a subtle but systematic trend in the positions of the intensity peaks. The intensity increment from the carbon peak to the first oxide peak (which represents single layers) is always slightly greater than the intensity increment to the second oxide peak (which represents double oxide layers). Subsequent intensity increments between peaks are constant, but the peaks themselves are frequently found to be broader than would be expected from the signal-to-noise statistics.

Figure 7 illustrates these discrepancies in more detail for an $n = 4$ sample. In this histogram (which was obtained under instrumental conditions different from those for Figure 4, so the intensities are scaled differently) the first
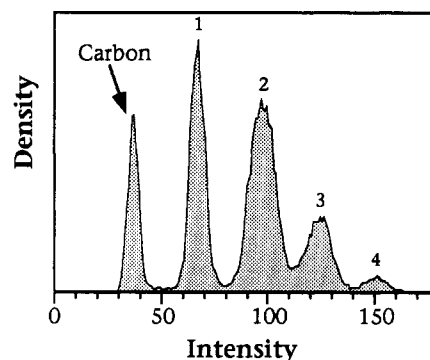

Figure 7. Intensity histogram of a HAAD image of exfoliated sheets of $K[Ca_2Na_{n-3}Nb_nO_{3n+1}]$, ($n = 4$) supported on amorphous carbon. Note the intensity step from the carbon peak to the first layer peak is slightly greater than subsequent intensity steps. Intensity peaks for the multiple layers are broader than would be expected from signal-to-noise considerations.

peak, corresponding to the support film, occurs at 36 intensity units. The intensity increments are thus 31 units for the step from 0 to 1 oxide sheet, 29 units for the step from 1 to 2 oxide sheets, and 28 units for the step from 2 to 3 oxide sheets.

Discussion

A plausible explanation for these discrepancies is that residual carbon, produced by the breakdown of surfactant during the specimen bake, is littered over all exposed surfaces of the specimen (see Figure 8). The total scattered intensity from a specimen region containing a single layer of oxide would have contributions from that single layer, two layers of residue (from the top and bottom of the oxide sheet), the carbon support film, and a third residue layer on the other side of the support film. For the second oxide peak there are two possibilities: either a bilayer of unexfoliated oxide or two single but overlapping layers of oxide. In the absence of detrital carbon, these two possibilities would scatter identical intensities. However, with carbonaceous deposits on all exposed surfaces, the overlapping layers offer extra exposed surfaces, relative to the unexfoliated bilayers. In the latter case, the interface between the upper and lower sheets will not contain any residue since no surfactant entered. We assume that unexfoliated bilayers do not exfoliate because they contain either no surfactant or an amount too small to permit layer separation during specimen preparation. The X-ray data indicate some inhomogeneity in the interlayer composition.

This interpretation is supported by comparing experimental intensity histograms between various regions in the image. Figure 9 shows a superposition of the histogram data in the vicinity of the broad double layer peak, from regions such as A and B in Figure 4b. Although both image areas appear to contain two sheets, the intensities from the two regions are not the same. The lower intensity peak comes from region A, which appears to be an unexfoliated double sheet (as judged by the fact that the two sheet edges are parallel). The higher intensity component comes from region B, which by inspection of the micrograph appears to contain two exfoliated monolayers (as judged by the fact that the sides of the sheets are misaligned). We propose that the difference in intensity is due to an extra layer of residue trapped between the two exfoliated sheets at B. Figure 4b reveals features on the platelets that resemble drying stains. These features are not bend contours, caused by changes in local diffraction conditions due to buckling of the sheets, since they do not move when the
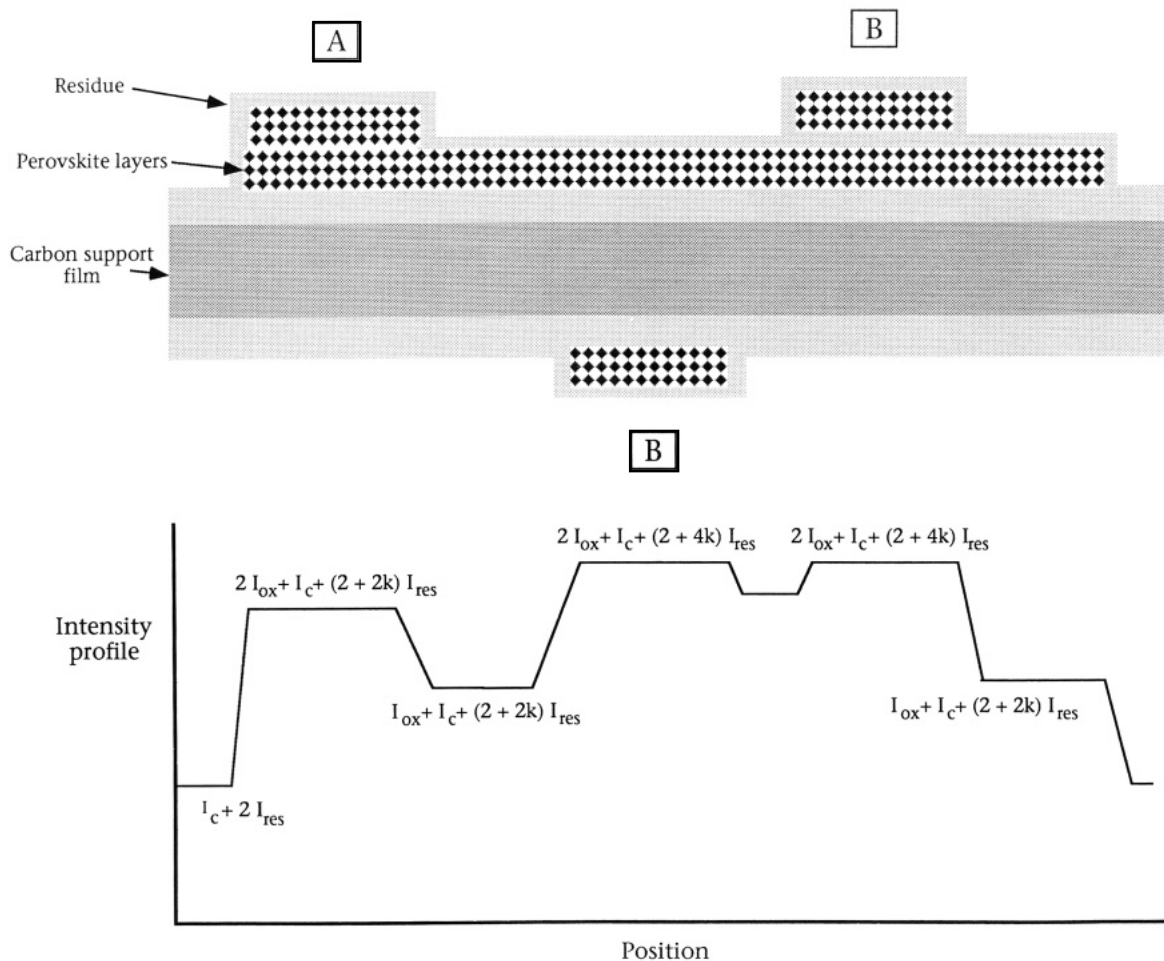
Figure 8. Sketch of the three distinct ways that two sheets can overlap in the specimens studied here. The intensity contribution from nonexfoliated bilayers (region labeled A) with generally be greater than the intensity from overlapping exfoliated sheets (regions labelled B).
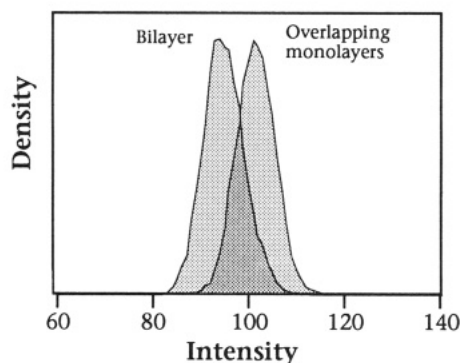
Figure 9. Superposition of intensity histogram data from HAAD image areas such as A and B in Figure 3b of the $n = 4$ material. Region A is a nonexfoliated bilayer and generates the lower intensity peak. Region B contains two overlapping single sheets and generates the higher intensity peak due to the extra layer of trapped residue.

specimen is tilted through ±5°. Differences in the amount of solid oxide deposited on each grid and hence in the amount of residue may explain why the support foil for the $n = 4$ material scattered ~20% more strongly than the support foil for the $n = 3$ material.

A simple formula for the intensity from an area of specimen containing $N_O (\geq 1)$ oxide sheets, of which N_{ex} of the $N_O - 1$ interfaces are exfoliated, is

$$I_{HAAD}(N_O) = N_O I_{oxide} + I_{carbon} + 2[1 + (N_{ex} + 1)k]I_{residue} \quad (4)$$

I_{oxide}, I_{carbon}, and $I_{residue}$ are the intensity contributions from

one layer of oxide, the carbon film, and one layer of residue on the carbon, respectively. We assume here that there is no residue between nonexfoliated sheets. The factor of 2 comes from counting the upper and lower surfaces of each distinct layer; $2(N_{ex} + 1)$ is the total number of exposed oxide sheet surfaces. k is a correction factor to allow for the possibility that any residue film attached to oxide sheets will not have the same thickness as residue deposited on a free carbon surface. A sketch of the physical relationship between carbon, oxide sheets, and residue is shown in Figure 8 for the case $N_O = 2$.

The intensity from the support film alone would be

$$I_{HAAD}(0) = I_{carbon} + 2I_{residue} \quad (5)$$

and from a single oxide layer is

$$I_{HAAD}(1) = I_{oxide} + I_{carbon} + 2(1 + k)I_{residue} \quad (6)$$

Applying eqs 5 and 6 to the data for the $n = 3$ and 4 materials produces a set of nonlinear equations relating I_{carbon}, k, $I_{residue}$ ($n = 3$), and $I_{residue}$ ($n = 4$). A unique solution to the problem is not obtained because, with the experimental data for $I_{HAAD}(1)$ and $I_{HAAD}(0)$ and the calculated numbers for I_{oxide}/I_{carbon} for each value of n (listed in Table II), two sets of values can be obtained and are listed in Table III. Although both are self-consistent, only one will be consistent with other intensity data.

The relevant set of values can be determined by analysis of the peak broadening (or splitting, in the case of Figure 9), which confirms that the first set of values apply in these experiments. The second set of values, representing a thicker residue, would produce much broader intensity

	solution 1		solution 2	
	$n = 3$	$n = 4$	$n = 3$	$n = 4$
$I_{residue}$	3.1	6.5	8.2	11.8
I_{carbon}	26	26	15.5	15.5
k	0.105	0.105	0.29	0.29

[a] Solution 1 is more consistent with other experimental data. I are given in arbitrary intensity units.

peaks for the multilayers than are observed. Relative to the intensity scattered by 20 nm of carbon, the first solution gives $I_{residue}$ ($n = 3$) $\approx 0.12 I_{carbon}$, $I_{residue}$ ($n = 4$) $\approx 0.25 I_{carbon}$, and $k \approx 0.1 I_{carbon}$ (with $I_{carbon} \approx 26$ intensity units). The second solution gives $I_{residue}$ ($n = 3$) $\approx 0.53 I_{carbon}$, $I_{residue}$ ($n = 4$) $\approx 0.76 I_{carbon}$, $k \approx 0.29 I_{carbon}$ (with $I_{carbon} \approx 15.5$ intensity units).

The first solution set implies that the thickness of the residue layer on the carbon is equivalent to ∼2.5 and ∼5 nm of carbon in the $n = 3$ and $n = 4$ materials, respectively. The thickness of the residue on each side of the oxide sheets is ∼0.25 nm, about one or two monolayers of carbon. Coarse estimates, based on figures for typical dispersion concentrations and volumes, give figures for the residue ranging from 1 to 100 nm (assuming all dispersed solids remain behind). It is no surprise that the two specimens have different residue thicknesses, since concentration and droplet volume were not controlled between samples. It is also no surprise that the calculations indicate that there is more residue on the $n = 4$ sample. Micrographs of this specimen showed more evidence of "drying marks" than the $n = 3$ specimen (compare parts a and b of Figure 4).

The analysis here implies that most of the residue is dispersed over the carbon, presumably through diffusion of breakdown products of the surfactant. Thus, in the experiment carried out here, the residue thickness is not a reliable indicator of the amount of surfactant originally associated with each face of the oxide sheets.

Summary

In this paper, the synthesis and exfoliation of layered perovskites was described together with a new imaging technique for characterizing the extent of the exfoliation. Oxide layer thickness is deduced from the intensity scattered into a high-angle annular detector in a scanning transmission electron microscope. The advantages of the technique over shadowing methods are that it is relatively insensitive to sheet buckling, it measures the thickness at all points on the sheet rather than only at the edge, and thickness distributions can be obtained directly from the intensity histogram of a single image.

The high-angle annular detector intensity data show that $H[Ca_2Na_{n-3}Nb_nO_{3n+1}]$ ($n = 3, 5$) can be exfoliated to the level of single sheets by preintercalation of a polyether amine surfactant. The fraction of monolayers observed in exfoliated samples varied with n. About 80% of the $n = 3$ sheets observed were monolayers. However, only about 50% of the $n = 4$ sheet area was completely exfoliated and less than ∼10% of the $n = 5$ sheets were true monolayers. Analysis of intensity histograms reveals small deviations from rigorously quantized intensity steps. This can be explained by the presence, on all exposed surfaces, of residual carbonaceous material, presumably originating from the breakdown of surfactant molecules when the specimen was baked.

Defect Level Identification in CuInSe₂ from Photoluminescence Studies

Geula Dagan,[†] F. Abou-Elfotouh,[‡] D. J. Dunlavy,[‡] R. J. Matson,[‡] and
David Cahen*,[†]

*The Weizmann Institute of Science, Rehovot, Israel 76100, and Solar Energy Research
Institute, Golden, Colorado 80401*

By correlating photoluminescence data with the electronic properties, stoichiometry, and chemical diffusion coefficients (of Cu) for a number of single-crystal samples, we arrive at a chemically and physically consistent interpretation of luminescent transitions in CuInSe₂. This interpretation involves point defect chemical assignments to the electron energy levels that are involved in these transitions. Thus the copper vacancy, V_{Cu}, is identified as a defect that is mainly responsible for Cu diffusion in this material. The electrochemical potential of the electron involved in the $V_{Cu}^x + e^- = V_{Cu}'$ reaction is found to be ca. 40 meV above the valence band.

Introduction

In the course of investigations on electronic effects of ion migration in I–III–VI₂ type semiconductors,[1] it became desirable to try to identify the chemical nature of dominant native defects in the CuInSe₂ samples that were studied. Results from a number of different experiments point to Cu as the most mobile species in CuInSe₂.[1–5] The most

obvious diffusion pathways for Cu are those that involve vacancies, V_{Cu}, and those that involve interstitials, Cu_i. In both cases the antisite defect, Cu_{In}, could be involved as

(1) Soltz, D.; Dagan, G.; Cahen, D. *Solid State Ionics* **1988**, *28–30*, 1105.
(2) Tell, B.; Wagner, S.; Kasper, H. M. *J. Electrochem. Soc.* **1977**, *124*, 536. Kasper, H. M.; Tell, B.; Wagner, S. U.S. Patent 4,115,633, 1978.
(3) Becker, K. D.; Wagner, S. *Phys. Rev.* **1983**, *B27*, 5240.
(4) Kleinfeld, M.; Wiemhöfer, H. D. *Ber. Bunsen-Ges. Phys. Chem.* **1986**, *90*, 711.
(5) Kleinfeld, M.; Wiemhöfer, H. D. *Solid State Ionics* **1988**, *28–30*, 1111.

[†] The Weizmann Institute of Science.
[‡] Solar Energy Research Institute.
* Author for correspondence.